Self-Assembly of Amphiphilic Hexapyridinium Cations at the Air/Water Interface and on HOPG Surfaces**

Haofei Gong,[a] Björn Bredenkötter,[a] Christoph Meier,[b] Carola Hoffmann-Richter,[b] Ulrich Ziener,[b] Dirk G. Kurth,[c] and Dirk Volkmer*[a]

Mono- and multilayers of a novel amphiphilic hexapyridinium cation with six eicosyl chains (3) are spread at the air/water interface as well as on highly ordered pyrolytic graphite (HOPG). On water, the monolayer of 3 is investigated by recording surface pressure/area and surface potential/area isotherms, and by Brewster angle microscopy (BAM). Self-organized tubular micelles with an internal edge-on orientation of molecules form at the air/water interface at low surface pressure whereas multilayers are present at high surface pressure, after a phase transition. Packing motifs suggesting a tubular arrangement of the constituting molecules were gleaned from atomic force microscopy (AFM) investigations of Langmuir–Blodgett (LB) monolayers being transferred on HOPG at different surface pressures. These LB film structures are compared to the self-assembled monolayer (SAM) of 3 formed via adsorption from a supersaturated solution, which is studied by scanning tunnelling microscopy (STM). On HOPG the SAM of 3 consists of nanorods with a highly ordered edge-on packing of the aromatic rings and an arrangement of alkyl chains which resembles the packing of molecules at the air/water interface at low surface pressure. Additional details of the molecular packing were gleaned from single-crystal X-ray structure analysis of the hexapyridinium model compound 2b, which possesses methyl instead of eicosyl residues.

Introduction

Ultrathin films of water insoluble organic molecules have been a topic of longstanding interest due to their potential applications in photonics, electronics, and catalysis.[1–6] To fabricate highly ordered ultrathin films, a critical issue is to control the supramolecular aggregation behavior of the constituting molecules at an interface. To date, the Langmuir–Blodgett (LB)[7] and the self-assembled monolayer (SAM)[8] approach, as well as layer-by-layer electrostatic self-assembly techniques[9] are the most successful methods for this purpose. The Langmuir–Blodgett technique allows one to fabricate ordered monolayers with some control over molecular orientation in a simple, yet highly efficient manner.[10] Another motivation for Langmuir monolayer investigations arises from the relationship between the structure and the functions of cell membranes in biological phenomena.[11] In addition, self-assembly of molecules on different substrate surfaces is an effective means to produce supramolecular patterns and packing motifs, for which noncovalent interactions such as electrostatic[12] and hydrophobic forces,[13] or hydrogen-bonding interactions[14] might be exploited. The supramolecular packing arrangement in a monolayer—after deposition onto a substrate via Langmuir–Blodgett film transfer—is often quite different from the corresponding structure of a self-assembled monolayer formed from solution. While the orientation of molecules in a monolayer spread at the air/water interface are mainly determined by hydrophobic interactions,[15] specific interactions between molecules and a substrate surface might predominate the formation of self-as-

sembled monolayers. Another difference pertaining to Langmuir monolayers is that different conformations of molecules within the film can be tuned not only by supramolecular self-organization, but also by adjusting surface pressure, subphase temperature, pH, and other experimental conditions. In contrast, the formation of self-assembled monolayers on solid substrates is mainly directed by the binding of the molecules to the substrate surface as well as by intermolecular interactions.[16]
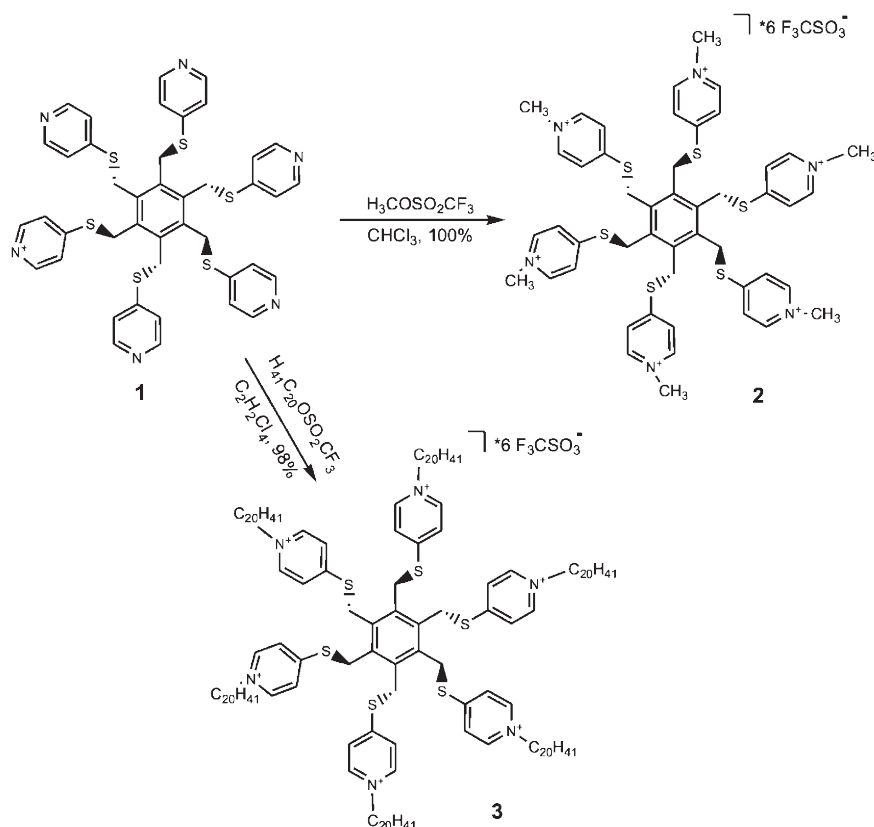
As an example for the self-assembly of highly charged molecules which are amphiphilic at the same time, we designed hexapyridinium cation (3) possessing six alkyl chains, as shown in Scheme 1. One of the incentives for preparing such compounds is to exploit their liquid-crystalline properties, both in

[a] Dr. H. Gong, Dr. B. Bredenkötter, Prof. Dr. D. Volkmer
Department of Inorganic Chemistry II, University of Ulm
89081 Ulm, Albert-Einstein-Allee 11 (Germany)
Fax: (+49) 731-502-3039
E-mail: dirk.volkmer@uni-ulm.de

[b] C. Meier, Dr. C. Hoffmann-Richter, Dr. U. Ziener
Department of Organic Chemistry III, University of Ulm
89081 Ulm, Albert-Einstein-Allee 11 (Germany)

[c] Dr. D. G. Kurth
Max-Planck Institute of Colloids and Interfaces, 14424 Potsdam (Germany)

Synthesis of the Pyridinium Triflate Salts

Compounds **2** and **3** were prepared by *N*-alkylation of hexakis (4-pyridylsulfanylmethyl) benzene **1**[21] with methyl- or eicosyl triflate, respectively (Scheme 1). Quantitative methylation was achieved by refluxing the reactants in chloroform for 5 h, whereas stirring for 15 h in tetrachloroethane at 100 °C with a slight excess of eicosyl triflate was necessary to obtain **3** in almost quantitative (98%) yield. Both compounds were characterized by ^1H and ^{13}C NMR spectroscopy as well as high-resolution electrospray ionization (ESI) mass spectrometry. The ^1H NMR spectra of **2** and **3** show two doublets for the pyridinium protons and a broad singlet for the thiomethylene group with the integral ratio 2:2:2. The N-methyl group of **2** shows a singlet at 4.81 ppm with integral 18 whereas the eicosyl group shows three triplets at 4.12, 1.67 and 0.65 ppm as well as a multiplet at 1.05 ppm with the integral ratio 2:2:3:34. The triflate anions in **2** and **3** are indicated in the ^{13}C NMR spectra by a quartet with $^1J_{C,F} = 319$ Hz at 120.4 ppm. The ESI mass spectrum of methyl triflate **2** shows threefold and twofold charged cations including four and three triflate anions, whereas the most stable ions of compound **3** are the fourfold and threefold cations including two or three triflate anions, respectively.

Single crystals of compound **2b** with the molecular formula $C_{48}H_{54}N_6S_6 \cdot (CF_3SO_3)_6 \cdot 2$ $CH_3OH \cdot H_2O$ were obtained by cooling a hot concentrated solution of **2** in methanol. All attempts to grow single crystals of compound **3**, suitable for single X-ray analysis, were unsuccessful so far.

Scheme 1. Synthesis of compounds **2** and **3** by sixfold *N*-alkylation of **1**.

Reaction conditions: $H_3COSO_2CF_3$, $CHCl_3$, 100%; $H_{41}C_{20}OSO_2CF_3$, $C_2H_2Cl_4$, 98%.

solution and in the solid state.[17] Compound **3** has a symmetric disc-like structure with cationic *N*-alkylpyridinium groups. Its amphiphilic characteristics results from six long-tailed hydrophobic eicosyl chains. Due to a high positive charge, **3** strongly interacts with anionic compounds such as simple monovalent counter anions, as shown herein, to yield rod-like structures at surfaces.

Disc-shaped molecules with a rigid core and flexible tails have been reported previously to form two-dimensional columnar phases at the air/water interface.[18] Such robust nonisotropic self-assembly behaviour would be highly desirable as a value-adding property for the fabrication of functional supramolecular structures, one particular example being surfactant-encapsulated clusters (SECs), which we have described previously. SECs are composed of anionic polyoxometalate clusters which are nested in a spherical shell of simple cationic surfactants.[19] SECs and likewise organic–inorganic composite materials have potential applications as electrochromic or photochromic devices and sensors.[20] However, the SECs described so far lack any propensity to form long-range-ordered nonisotropic structures, for the fabrication of which disc-shaped compounds such as **3** might be required. We discuss the formation of robust tubular micelles of **3** at the air/water interface and on solid substrates. We demonstrate that structurally robust supramolecular nanorods with an internal edge-on arrangement of disc-shaped molecules form on a HOPG surface, a self-assembly process which is independent of film formation or transfer method.

Micelle Formationat the Air/Water Iterface

Compound **3** was spread as a monolayer at the air/water interface. The putative conformation and orientation of molecules in the monolayer are investigated by surface pressure/area and surface potential/area isotherms, as well as by in situ Brewster angle microscopy, and ex situ atomic force microscopy (AFM) measurements. Figure 1 shows the surface pressure/area and the surface potential/area isotherm of **3** spread on pure water at room temperature, as well as the surface pressure/area hysteresis curves corresponding to different target pressures. The surface pressure-area isotherm indicates two structurally different liquid condensed phases separated by a phase transition.
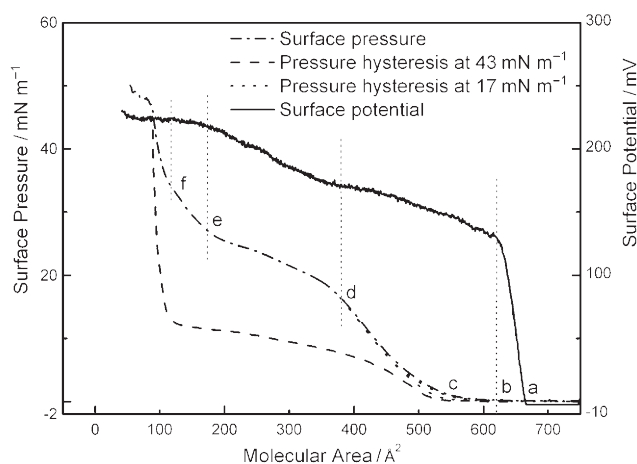
Figure 1. Surface pressure/area and surface potential/area isotherms of **3** on a pure water subphase at 20 °C. The dotted and dashed lines indicate the surface pressure/area decompression isotherm immediately after compressing the monolayer to the target pressure of 17 and 43 mN m⁻¹, respectively. Points (a–f) in the isotherm indicate the following: a) onset of surface potential; b) steadily increasing surface potential; c–d) liquid-expanded monolayer; d–e) phase transition; f) liquid-condensed monolayer.

The monolayer isotherm shows its onset pressure at a molecular area of about 580 $Å^2$ per molecule (as indicated by point (c) in Figure 1).

It is proposed that already at low surface pressure the molecular components of **3** adopt a packing in the monolayer which resembles its solid-state structure. From the single-crystal X-ray diffraction data of the methyl substituted analogue **2 b** (see Supporting Information), which forms a close packing in the *ab*-plane of the crystal lattice, it is reasonable to deduce that the eicosyl derivative **3** may self-assemble into a close-packed arrangement of charged groups (pyridinium and triflate moieties) at the air/water interface. At a surface area larger than 580 $Å^2$ the molecules might lay flat (face-on) or tilted (edge-on) on the water surface, which can hardly be distinguished from isotherm data because of the unknown orientations of alkyl chains. After onset of pressure at 580 $Å^2$, the isotherm of **3** shows a liquid expanded and a liquid condensed phase. At about 400 $Å^2$ per molecule (at $\pi = 17$ mN m⁻¹, indicated as point (d) in Figure 1), the isotherm shows a phase transition leading to the liquid condensed phase. Extrapolating the isotherm from the high-pressure region towards zero surface pressure (that is, drawing a straight line between point (f) and the point corresponding to 48 mN m⁻¹, at which monolayer collapse occurs) leads to an area of 170 $Å^2$. This area value is far too small to assume for a monolayer arrangement of **3**; it is thus proposed that a multilayer forms at high surface pressure ($\pi > 30$ mN m⁻¹).

To gain further insights into the dynamics of the pressure-dependent positional rearrangement of molecules in the monolayer, a surface potential/area isotherm and the surface pressure/area isotherm were recorded simultaneously. Several particular features were observed in the curves as shown in Figure 1.

Firstly, there is a critical area at which the surface potential increases steeply. This area is between 650 and 750 $Å^2$ based on several independent measurements. At an area larger than 750 $Å^2$, the molecules have enough space to move freely at the water surface, on which they form discontinuous monolayer patches. These patches have a rather large distance from each other and can only be detected when they occasionally pass by the surface potential electrode. However, upon compressing the monolayer to 650–750 $Å^2$, these film patches are driven together and a reliable and stable surface potential can be measured.

Upon further compression ($A < 620$ $Å^2$) the increase of surface potential is less steep but discernible, although the surface pressure does not change significantly. It is also noted that the initial area at the onset of the surface potential increase is much larger than the corresponding value at the onset of the surface pressure, that is, 580 $Å^2$ per molecule. This might be due to the fact that the surface pressure/area isotherm is closely related to short-range van der Waals interactions between the hydrocarbon chains of the molecule, whereas the surface potential/area isotherm is related to the long-range dipole–dipole interactions between the polar head groups.[22]

At point (b) of the isotherm, the corresponding surface potential is about 130 mV, which is a relatively low value if compared to the surface potential of monofunctional charged surfactants such as arachidic acid.[23] Since the surface potential is a quantitative means of the average dipole moment of the monolayer, we conclude that compound **3** predominantly forms a nondissociated monolayer at the air/water interface, since a quantitative dissociation into (water-insoluble) cations and (water-soluble) anions should lead to a highly polar monolayer structure. Therefore, the intermolecular interactions between the molecules in the monolayer of **3** at this point of the isotherm are predominantly governed by π–π interactions and hydrophobic interactions.

Secondly, the surface potential shows a steady increase between b and d. The surface potential ($\triangle V$) of a monolayer spread at the air/water interface has frequently been interpreted in terms of Equation (1):[24]

$$\mu_\perp = A \triangle V / 12\pi \tag{1}$$

where A is the molecular area ($Å^2$ per molecule), and $\mu_\perp$ is the surface dipole moment for nonionized monolayers, which is used to describe the molecular orientation in a film. A steady increase of the surface potential might be indicative of a slight change of the molecular dipole moments at direction normal to the air/water interface.[25] It is thus assumed that the positions of the charged hydrophilic core and the counter anions do not change significantly between the points (b) and (d) of the isotherm. The slight change of the surface potential may thus attribute to changes of the conformations of alkyl chains upon compression.
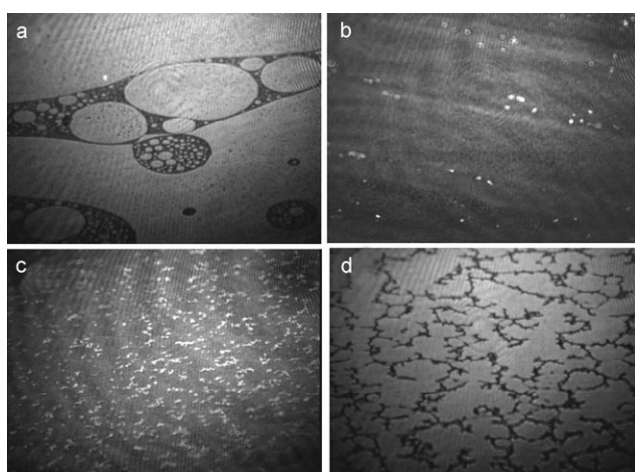
Thirdly, there is a relatively steep increase of the surface potential during phase transition, that is, from point (d) to (e) of

the isotherm, which may indicate progressive formation of a double or multilayers.

Lastly, it is also noted that there is a short plateau in the surface potential curve [left of point (f)], indicating the formation of an almost incompressible multilayer that cannot adapt its structure to the external pressure via further conformational or positional changes.

The two different physical states of **3**, that is, before and after phase transition, can also be verified by the hysteresis that the monolayer exhibits at different compression states, as shown in Figure 1. Hysteresis indicates an irreversible phase transition or chemical reaction in the monolayer. If the monolayer is compressed at a maximum of $\pi = 17$ mN m^{-1} (the pressure being still below the phase-transition point), the isotherm shows almost no hysteresis after two compression and expansion cycles, which suggests that the structural changes in the monolayer are completely reversible and fast. This behaviour provides a further impetus to our previous statement that the compression in the low-pressure phase of the monolayer mainly affects the conformation of alkyl chains of **3**. In comparison, a large hysteresis was observed if the monolayer was cyclically compressed and expanded between 0 and 43 mN m^{-1}, which strongly indicates an irreversible formation of multilayers at high surface pressure after phase transition.

Further information about film morphology was gleaned from Brewster angle microscopy (BAM). BAM images were recorded at different surface pressures from a monolayer of **3** spread on pure water, as shown in Figure 2. At zero pressure (before compression), highly mobile circular domains were observed (Figure 2a), which float rapidly at the air/water interface. These round domains were pushed together and fused to form a homogeneous monolayer upon compression before the phase transition stage. At the middle of the phase transition plateau, for example, at $\pi = 20$ mN m^{-1}, some aggregates appearing as little bright spots were formed in the homogene-
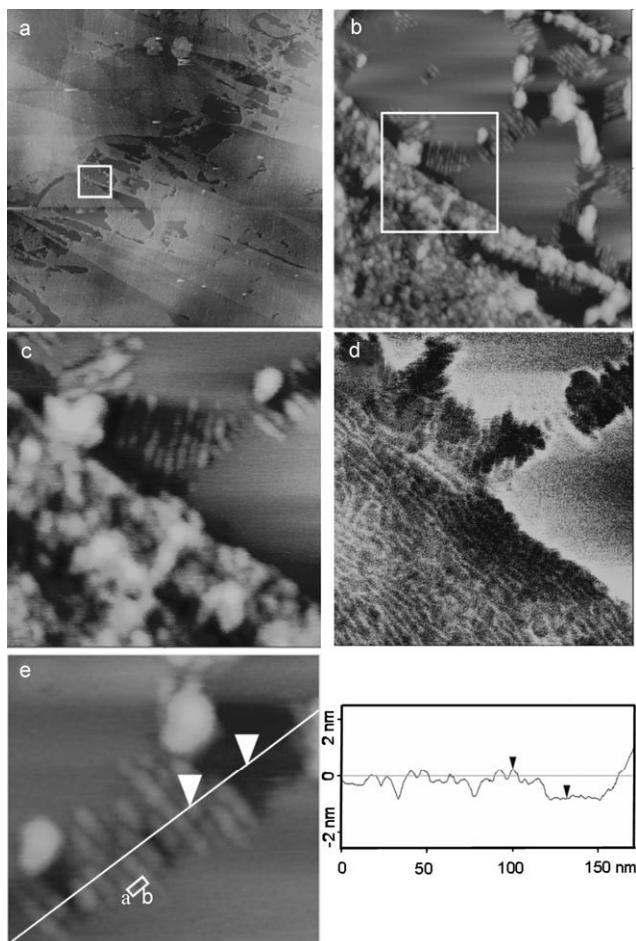
ous monolayer (Figure 2b), indicating the beginning of multilayer formation at this pressure. The initial round domains can be obtained again if the monolayer is decompressed from this state. Eventually, increasing numbers of dot-shaped aggregates cover the entire surface and thus lead to a grainy film morphology that appears brighter and thicker after having passed the phase transition plateau, as shown in Figure 2c. Expanding the monolayer from this stage, the film disintegrates into irregular domains, indicating that the multilayer decomposes irreversibly into smaller multilayer patches and domains rather than to return to the monolayer state as discussed above (Figure 2d).

The BAM measurements are in complete agreement with the monolayer phase behaviour of **3** as gleaned from isotherm data. The occurrence of a thick and spotted layer at high surface pressure suggests that the monolayer transforms into a multilayer. At no point of the isotherm did the BAM images give any signs of long-range order in the monolayer, that is, the formation of a liquid-crystalline phase, which would be discernible by a characteristic optical texture. Therefore, the phase transition is indicated in the BAM micrographs only by a slight change in the average brightness of the monolayer. However, due to the inherent physical limitations of the lateral optical resolution of BAM, we cannot rule out the existence of crystalline domains with domain sizes smaller than 1 μm in the high-pressure phase.

AFM Measurement of the Transferred LB Film

Obviously, there is a distinctive structural change before and after phase transition in the π/A isotherms. To further reveal the molecular packing at the air/water interface, film structures were imaged by AFM for Langmuir–Blodgett films transferred onto HOPG substrates at low and high surface pressure. AFM images of the LB film transferred at 10 mN m^{-1} show a striped phase morphology, although the HOPG surface was not fully covered by the monolayer as shown in Figures 3a and 3b. The tubular phase was clearly discernible over the whole image area, details of its internal composition, however, became much clearer in the phase image (Figure 3d), indicating the formation of tubular or rod-like micelles at low surface pressure. Comparing these results with the dimensions of **3** depicted in Scheme 2 and taking the STM results discussed below into account, it is reasonable to assume that the molecules adopt an edge-on orientation with respect to the air/water interface (or the HOPG substrate, respectively), where the charged pyridinium moieties and the counter anions represent the longitudinal core of the elongated tubular micelles, from which the hydrophobic eicosyl chains extend into space, as proposed in Scheme 3.

The average distance between adjacent nanorods is 6.6–7.1 nm, as measured from a topographic AFM image (Figure 3e), which is consistent to the molecular diameter of **3** assuming fully extended alkyl chains. The average thickness of a monolayer of these rods, however, amounts to about 1 nm only, which fits very well to the diameter of the inner benzene core, as shown in Scheme 2. The tubular micelles are thus flat-

Figure 2. Brewster angle microscopy (BAM) images recorded for a monolayer of **3** spread on a pure water subphase at: a) 0 mN m^{-1} (shortly after spreading), b) 20 mN m^{-1} in the middle of the phase transformation, c) 35 mN m^{-1} after phase transformation, and d) 0 mN m^{-1} after expansion of the monolayer from 43 mN m^{-1}.

Figure 3. AFM images of an LB film of **3** transferred onto a HOPG substrate at $\pi = 10$ mN m^{-1}. Dimensions of imaged areas are a) 5 µm×5 µm, b) 500 nm×500 nm, c) 200 nm×200 nm [height image] and d) 200 nm×200 nm [phase image] e) Magnified part of the image (c).

tened in the *z*-direction, while within the micelles molecules are packed side by side, thus maximizing π–π and hydrophobic interactions. If we assume that the intermolecular distance is 0.7 nm, as derived from STM investigations (see below), the space requirement per molecule can be estimated to some 460–500 Å^2. This value closely matches the molecular area at 10 mN m^{-1} from the surface pressure/area isotherm (see above).

The LB film at $\pi = 35$ mN m^{-1}, that is, after the phase transition, shows a somewhat different characteristic morphology with an average film thickness of 4–5 nm. This increase of thickness is ascribed to the formation of a multilayer during compression, rather than to a positional rearrangement of the molecules: the formation of a multilayer is strongly suggested by AFM height profile measurements, in which discrete height steps at integer multiples of 1.1–1.2 nm (Figure 4) frequently occur. Each step height compares to the height of the LB monolayer at low surface pressure (see above). These data are also consistent with the BAM images, where the appearance of dotted aggregates at the beginning and after the phase transition was attributed to multilayer structures.

Similar disc-shaped molecules or macrocycles have been studied previously, and a positional change of the macrocycles from a face-on to an edge-on orientation with respect to the air/water interface upon monolayer compression has been suggested.[26] Our results, however, indicate the formation of tubular micelle structures even at the beginning of compression, which seems to be energetically favorable for the self-assembly of compound **3**. From these findings it is assumed that the intermolecular interactions between the macrocyclic molecules and the counter anions of **3** are much stronger than their interaction with water, which leads to an edge-on orientation even at the beginning of the spreading process.

Additional AFM investigations (not shown) were undertaken to enlighten the influence of the substrate on the morphology of the monolayers. Hence, monolayers of **3** were transferred onto mica and silicon under the same conditions as on HOPG. It turned out that the morphology of the organic layers at high transfer pressure (35 mN m^{-1}) closely resembles that on HOPG and thus does not depend on the nature of the substrate. At low transfer pressure (10 mN m^{-1}), in contrast to the experiments using HOPG, no structured film regions could be detected neither on silicon nor on mica. We attribute this to the intrinsic roughness of silicon (about 1 nm) on the one hand, and the strong interactions of the highly polar charged surface of mica with the charged molecules of **3**, on the other.

Self-Assembly on HOPG Surfaces

To get more information about the arrangement of the molecules in the monolayer, submolecular resolution in microscopic images is required. Therefore, a LB monolayer of **3** was deposited onto HOPG at low surface pressure (7 mN m^{-1}) and investigated by STM. Measurements on a dry film did not lead to structurally resolved STM images. Only after treating the substrate covered with the LB film with a drop of chloroform could the resulting monolayer be imaged in 1,2,4-trichlorobenzene (TCB) by STM; the result is shown in Figure 5a. Through the addition of CHCl$_3$, which is a reasonable solvent for **3**, the molecules gain flexibility at the CHCl$_3$/HOPG interface and can thus optimize their intermolecular interactions and their interaction with the HOPG substrate. As a result of this relaxation of the precursor LB film, the monolayer can be imaged by STM. In addition, the deposition of compound **3** was successful from a diluted chloroform solution. Imaging of the molecular monolayer succeeded again after adding a drop of TCB to the modified substrate. A typical STM image of the resulting monolayer is shown in Figure 5b.

On the HOPG surface, the molecules are ordered into a highly oriented structure with elongated rod-like domains. The brighter parts in the STM image in Figure 5a clearly show the eicosyl chains of **3** at nearly submolecular resolution, whereas the dark stripes can be assigned to the central aromatic part of the molecules. Additionally, the topographic STM image in Figure 5b reveals the aromatic core part of **3**. In both types of images, the distances between adjacent rods are $a = 4.31 \pm 0.08$ nm and $b = 0.70 \pm 0.03$ nm, respectively, enclosing an angle of $83 \pm 1°$. Therefore, the packing density is approxi-
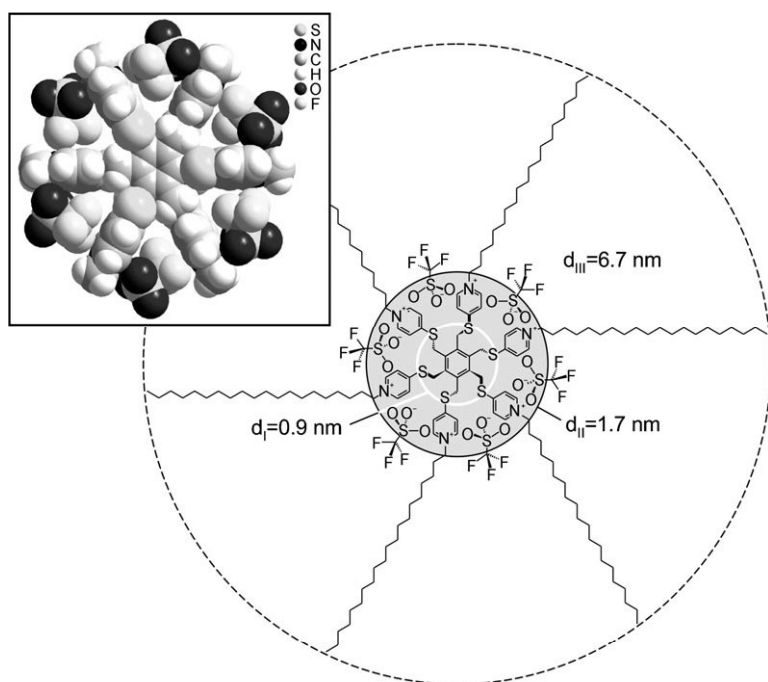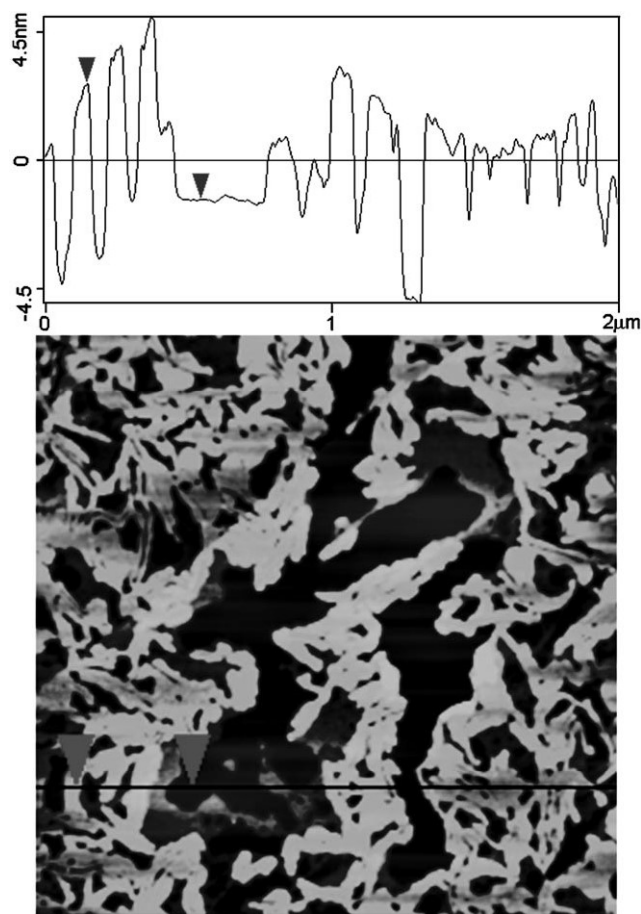
Scheme 2. Structural drawing of compound **3**, indicating structurally different cross-sectional levels of the molecule estimated from a molecular model which is derived from the crystal structure of compound **2b**. d_I refers to the diameter of the inner rigid benzene moiety, and d_{II} refers to the diameter of the charged core. d_{III} refers to the maximum extension of a single molecule assuming that the C_{20} alkyl chains adopt a fully stretched (all-*trans*) conformation. The inset shows a space-filling model of the packing arrangement of cations and anions in the crystal lattice of **2b**.
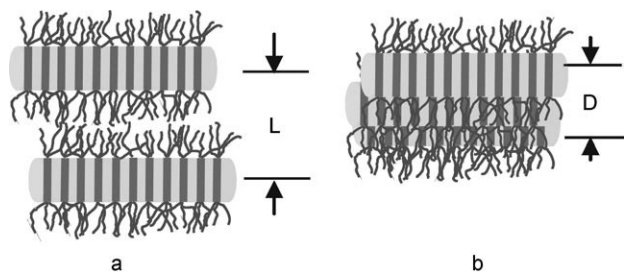

Scheme 3. Model of the supramolecular packing arrangement of **3** before (a) and after (b) phase transition at the air/water interface. Thick lines represent the central, charged part of **3**, whereas the thin lines symbolize the alkyl chains. L indicates the distance between adjacent nanorods of 6.6–7.2 nm. D indicates the thickness of the multilayers of 4–5 nm.

the rod axis with the central phenyl rings lying parallel to each other. Our prediction is that the four remaining alkyl chains will extend into the supernatant solution and play, therefore, a minor role for the stabilization of the monolayer. Hence, they are fairly flexible and cannot be imaged by STM. Such dangling chains are already known in the literature.[28–31] The physisorbed non-interdigitating alkyl chains are not as densely packed as seen in other alkyl-substituted molecules[32] or halogen-substituted alkanes.[33] In the molecular monolayer of the eicosyl-substituted hexapyridinium cations, the alkyl–alkyl distance is about 0.63 nm, whereas densely packed alkyl chains commonly show an interalkyl distance of 0.45 nm.[27] An ex-

mately 0.33 molecules nm^{-2}. The eicosyl chains enclose an angle of $60 \pm 1°$ to the rod axis, which corresponds to the well-known commensurable adsorption geometry of alkyl chains on graphite.[27] The rod structure in the STM images resembles strongly the morphology found in the AFM images (Figure 3). The smaller width of one rod in the STM images compared with the value obtained from AFM images is attributed to the fact that the alkyl chains form an angle with the main axis of the tubular micelle. Hence, we propose that the molecules are standing upright on the graphite substrate with two eicosyl chains per molecule adsorbed on the substrate (Figure 6). In this model, the molecules are arranged in a perfect row along

Figure 4. AFM images of an LB film of **3** transferred onto a HOPG substrate at $\pi = 35$ mN m^{-1}. The image size is 2 μm × 2 μm.
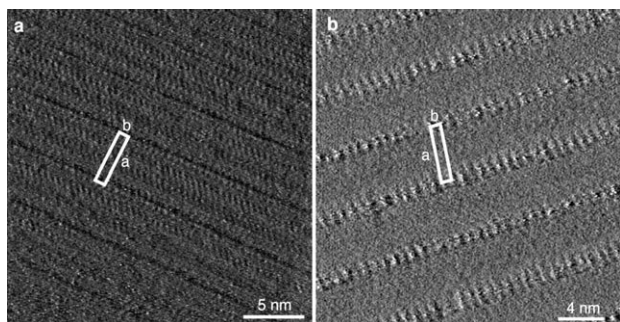
Figure 5. a) STM image of an LB film of **3** on HOPG, imaged in TCB after the addition and evaporation of chloroform revealing the crystallized alkyl chains of the investigated molecules. Constant-height mode, $I_T = 4.4$ pA, $U_T = -876$ mV. b) STM image of **3** deposited from a chloroform solution and imaged in TCB after evaporation of chloroform revealing the aromatic part of **3**. Constant-current mode, $I_T = 22$ pA, $U_T = -455$ mV. The given periodicities in both images are identical.
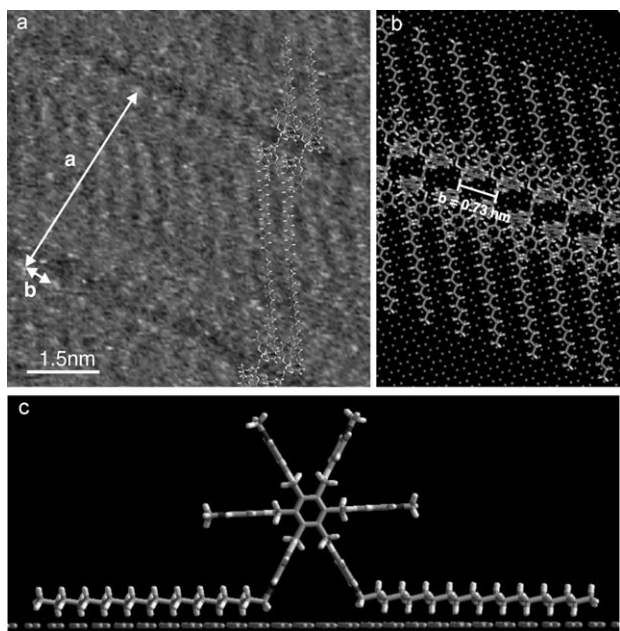
Figure 6. a) Magnified area of the STM image shown in Figure 5 with a superimposed schematic molecular model. b) Schematic model of a single nanorod. The molecules are arranged on the substrate in a row along the rod axis. c) View along the rod axis. Two eicosyl chains are adsorbed on the graphite substrate; the remaining four eicosyl chains are not shown for clarity and are proposed to extend into the supernatant solution.

planation for this exceptional behaviour can be found in the steric requirements of the core of the molecules, which drives the alkyl chains into an expanded arrangement with weaker interalkyl van der Waals interactions. Furthermore, the alkyl chains expanding into the supernatant solution are fairly flexible. These dangling alkyl chains complicate the imaging of the alkyl chains crystallized on the HOPG surface, which then might appear broader than submolecularly resolved alkyl chains. It should also be mentioned that the conformation of the pyridinium cations of **3**, which is used in the proposed

model, is the best compromise of ideal intramolecular bond angles and adsorption geometry on the graphite surface.

The position of the triflate counter ions of **3** in the monolayer cannot be deduced directly from the STM images. Nevertheless, there is enough space for the counter ions to become positioned at close proximity to the pyridinium cations to reduce electrostatic repulsion and to ensure charge compensation in the monolayer, as we can derive from a packing analysis of compound **2b** in its solid state (see Supporting Information).

Conclusions

In summary, an amphiphilic hexapyridinium cation (**3**) with six alkyl chains was synthesized and spread as a monolayer at the air/water interface. The molecules form interfacial micellar structures with an edge-on coplanar orientation of their rigid cores at the beginning of compression as revealed by AFM measurements. A phase transition occurs in the pressure regime from 17 to 28 mN m^{-1}, which is ascribed to formation of a multilayer, based on AFM, BAM images, and the analysis of the Langmuir and surface potential isotherms.

Compound **3** also forms highly ordered molecular nanorods in which the molecules are packed into an edge-on arrangement on HOPG upon self-assembly from a solution. The fact that **3** shows an edge-on orientation of molecules both at the air/water interface as well as on HOPG surfaces suggests strong intermolecular interactions between the charged components of **3**. However, a highly ordered two-dimensional packing of **3** can only be observed in the self-assembled films on HOPG surfaces, indicating that the substrate molecule interactions (van der Waals) play an important role in determining the packing of alkyl chains.

These experimental findings indicate that charged disc-like molecules such as **3** might be used as structurally robust supramolecular synthons for the reliable self-assembly of rod-like structures. Investigations on hybrids of the pyridinium hexacation with anions such as polyoxometalate clusters are underway to gain further insights into the self-assembly process.

Experimental Section

General: Hexakis(4-pyridylsulfanylmethyl)benzene (**1**) was prepared as described in the literature.[21] Eicosyl trifluoromethanesulfonate was synthesized by a procedure analogous to the one described for dodecyl trifluoromethanesulfonate in the literature.[34]

Melting Points (Uncorrected): Büchi Melting Point B-540 apparatus. Infrared (IR) spectra: Bruker FTIR IFS 113v spectrometer; KBr pellets. Nuclear magnetic resonance (NMR) spectroscopy: Bruker DRX 500 or Bruker Avance 400; data given as ppm; spectra referenced to the residual solvent peak; the degree of substitution of C atoms was determined by the distortionless enhancement by polarization transfer (DEPT-135) method. ESI mass spectra: Fourier transform ion cyclotron resonance (FT-ICR) mass spectrometer APEX III (Bruker) equipped with a 7.0 T 160-bore superconducting magnet (Bruker), infinity cell, and interface to an external (nano)ESI source. Elemental analyses were performed at the Micro Analytical Section of the University of Ulm. Kugelrohr distillation: Büchi Glas oven

model B-585. Thin-layer chromatography: silica gel (Kieselgel F_{254}) on Al foil (Merck). Gravity column chromatography: silica gel (Kieselgel 60, $\varnothing = 0.063$–0.200 mm, Merck). All solvents were purified by distillation before use and dried according to standard procedures when necessary.

Synthesis of Hexakis[(1-methyl)4-pyridyliumsulfanylmethyl]benzene Triflate (2): A solution of 50 mg (61 µmol) hexakis(4-pyridylsulfanylmethyl)benzene (1)[21] and 10.5 mg (64 µmol) methyl trifluoromethane sulfonate in 5 mL dry chloroform was refluxed for 5 h. The solvent and excess methyl triflate was removed by Kugelrohr distillation in vacuum at 50 °C, leading to the pure compound 2 as a colorless solid in quantitative yield. Melting point: 232–239 °C (dec.). ^{1}H NMR (400 MHz, [D$_4$]MeOH): $\delta = 8.49$ (d, $J = 7.1$ Hz, 12 H), 7.88 (d, $J = 7.1$ Hz, 12 H), 4.88 (s$_{br}$, 12 H), 4.21 (s, 18 H). ^{13}C NMR (100 MHz, [D$_4$]MeOH): $\delta = 161.2$, 143.2, 122.8, 120.4 (q, 319 Hz), 46.2, 30.7. $C_{48}H_{54}N_6S_6 \cdot (CF_3SO_3)_6$; MS (ESI, positive ions): $m/z = 451.043$ [M + 3 triflate]$^{3+}$, 751.039 [M + 4 triflate]$^{2+}$.

Single crystals (2b) with the molecular formula $C_{48}H_{54}N_6S_6 \cdot (CF_3SO_3)_6 \cdot 2CH_3OH \cdot H_2O$ were obtained by slowly cooling a hot concentrated solution of 2 in methanol.

Synthesis of Hexakis[(1-eicosyl)4-pyridyliumsulfanylmethyl]benzene Triflate (3): A solution of 135 mg (165 µmol) hexakis(4-pyridylsulfanylmethyl)benzene (1)[21] and 578 mg (1.34 mmol) eicosyl trifluoromethane sulfonate in 10 mL dry tetrachloroethane was stirred at 100 °C for 15 h. The solvent was removed by Kugelrohr distillation in vacuum at 50 °C. The residue was purified by column chromatography (CHCl$_3$ → CHCl$_3$/MeOH 4:1) resulting in a colorless oil. An amorphous colorless solid was obtained after treatment with methanol. Yield: 552 mg; 98 %. Mp.: 237–241 °C (dec.). ^{1}H NMR (400 MHz, CDCl$_3$/[D$_4$]MeOH 2:1): $\delta = 8.21$ (d, $J = 7.1$ Hz, 12 H), 7.60 (d, $J = 7.1$ Hz, 12 H), 4.59 (s$_{br}$, 12 H), 4.12 (t, $J = 7.4$ Hz, 12 H), 1.67 (t, $J = 6.6$ Hz, 12 H), 1.05 (m, 204 H), 0.65 (t, $J = 7.1$ Hz, 18 H). ^{13}C NMR (CDCl$_3$/[D$_4$]MeOH 4:1, 125 MHz, ppm): $\delta = 164.4$, 145.2, 139.2, 126.6, 120.4 (q, 319 Hz), 63.9, 34.9, 34.1, 32.70, 32.65, 32.61, 32.5, 32.4, 32.0, 29.2, 25.7, 17.0. $C_{162}H_{282}N_6S_6 \cdot (CF_3SO_3)_6$; MS (ESI, positive ions): $m/z = 700.745$ [M + 2 triflate]$^{4+}$, 983.645 [M + 3 triflate]$^{3+}$.

Langmuir Monolayer Investigations: Measurements of surface pressure per area (π/A) isotherms and LB film transfers were carried out on a double barrier NIMA rectangular trough. The surface pressure of the monolayers was measured using a filter paper Wilhelmy plate. The Langmuir film of 3 was formed by spreading a chloroform solution (2×10^{-4} mol L^{-1}) onto deionized purified water ($\rho >$ 18 MΩ cm). After evaporation of the solvent (approx. 15 min), the π/A isotherms of the spread films were recorded at room temperature (20 °C) by compressing the Langmuir film at a barrier speed of 15 cm^{2}min^{-1}. Hysteresis effects were investigated by means of recording Langmuir isotherms for repeated compression/expansion cycles. Surface potential measurements were performed with a Trek electrometer. A vibrating electrode was placed about 2 mm above the air/water interface and the reference electrode (a stainless-steel plate) was immersed in the subphase.

Brewster Angle Microscopy (BAM): Brewster angle microscopy was performed with a NIMA Langmuir trough (NIMA 702BAM) using a BAM-2 (I-Elli2000 supplied by NFT, Nanofilm Technology, Göttingen, Germany). Images of the film were recorded with a lateral resolution of 2 µm. The size of each BAM image corresponds to a monolayer area of 430 µm in width.

Atomic Force Microscopy (AFM): A single layer of the LB film was transferred onto a HOPG substrate by the vertical lifting method (both at low and high surface pressures). The HOPG substrate was immersed into the water subphase before monolayer spreading.

After monolayer spreading and compression to a certain target pressure, a single layer of the monolayer was transferred onto the substrate by lifting off the substrate at a speed of 5 mm min^{-1}. The morphology of the transferred Langmuir–Blodgett (LB) film was observed by atomic force microscopy (Nanoscope IIIa, Digital Instruments).

Scanning Tunnelling Microscopy (STM): The STM experiments were performed under ambient conditions with a low-current RHK 1000 system. Distances were calibrated by measuring the interatomic distances of highly ordered pyrolytic graphite (HOPG, SPI). After imaging a freshly cleaved HOPG substrate with atomic resolution to ensure a high tip quality, the tip was brought into tunnel contact with the sample coated with the Langmuir–Blodgett (LB) Film. After adding a drop of chloroform (Aldrich) and evaporation of the solvent, a drop of 1,2,4-trichlorobenzene (TCB, Aldrich) was added to the sample to remove impurities. The deposition from a diluted chloroform solution was accomplished as follows: first, the HOPG substrate was imaged with atomic resolution; secondly, a drop of a diluted solution of 3 in chloroform was applied to the substrate with the tip in tunnel contact. After evaporation of the solvent, a drop of TCB was added to the substrate. All STM images were recorded with a resolution of 512×512 points. The scan speeds varied from 0.2 to 0.6 µm s^{-1} using mechanically sharpened Pt/Ir (80/20) tips. The presented STM images have not been subject to any image manipulation or processing. The proposed models where created with Hyperchem molecular modeling software [Hyperchem V7.01, Hypercube Inc., 2002] through a combination of geometry optimizations with the built-in force field and manual adjustments.

X-ray Crystallography: Single-crystal X-ray diffraction data were collected at 220 K on a Stoe imaging plate diffraction system (IPDS) diffractometer employing monochromatic Mo-K_α radiation ($\lambda = 0.71073$ Å). The initial structure of 2b was solved by direct methods and refined by full-matrix least-squares techniques based on F^2 using the SHELXL-97 program.[35] All non-hydrogen atoms were refined anisotropically. Hydrogen atoms were placed at calculated positions and refined using a riding model. Details of data collection and refinement of the compound are summarized in Table S1 (in Supporting Information). Complete X-ray data including tables of atom coordinates, bond distances, and angles are also given in the Supporting Information.

Acknowledgements

[1] A. Ulman in *An Introduction to Ultrathin Organic Films—From Langmuir–Blodgett to Self-Assembly*, Academic, San Diego, 1991.

[2] J. H. Fendler in *Membrane Mimetic Chemistry: Characterizations and Applications of Micelles,Microemulsions,Monolayers,Bilayers,Vesicles,Host-Guest Systems,and Polyions* , Wiley-Interscience, New York, **1982**.

[3] J. M. Lehn in *Supramolecular Chemistry*, VCH, Weinheim, **1990**.

[4] C. Floriani, A. E. Merbach in *Perspectives in Coordination Chemistry* (Ed.: A. F. Williams), VCH, Weinheim, **1992**.

[5] V. Balzani, A. Juris, M. Venturi, S. Campagna, S. Serroni, *Chem. Rev.* **1996**, *96*, 759.

[6] F. Caruso, *Top. Curr. Chem.* **2003**, *227*, 145.

[7] a) G. G. Roberts in *Langmuir–Blodgett Films*, Plenum, New York, **1990**; b) C. M. Petty in *Langmuir–Blodgett Films,An Introduction* , Cambridge University Press, Cambridge, **1996**.

[8] R. Maoz, R. Yam, G. Berkovic, J. Sagiv in *Thin Films,Vol. 20: Organic Thin Films and Surfaces: Directions for the Nineties* (Ed.: A. Ulman), Academic, New York, **1995**.

[9] G. Decher, *Science* **1997**, *277*, 1232.

[10] M. Seul, D. Andelman, *Science* **1995**, *267*, 476.

[11] J. M. Lehn, *Science* **2002**, *295*, 2400.

[12] Y. Liu, ; Y. Wang, H. Lu, R. O. Claus, *J. Phys. Chem. B.* **1999**, *103*, 2035.

[13] Z. Tang, W. Jing, E. Wang, *Langmuir* **2000**, *16*, 1696.

[14] Y. Fu, H. Chen, D. Qiu, Z. Wang, X. Zhang, *Langmuir* **2002**, *18*, 4989.

[15] K. B. Blodgett, *Phys. Rev.* **1937**, *57*, 964.

[16] a) R. G. Nuzzo, F. A. Fusco, D. L. Allara, *J. Am. Chem. Soc.* **1987**, *109*, 2358; b) R. G. Nuzzo, L. H. Dubois, D. L. Allara, *J. Am. Chem. Soc.* **1990**, *112*, 558; c) G. M. Whitesides, P. E. Laibins, *Langmuir* **1990**, *6*, 87.

[17] B. Binnemans, *Chem. Rev.* **2005**, *105*, 4148.

[18] a) D. Gidalevitz, M. L. Kurnaz, O. Y. Mindyuk, B. M. Ocko, D. K. Schwartz, P. A. Heiney, *Langmuir* **1998**, *14*, 2910; b) J. Malthete, D. Poupinet, R. Vilanove, J.-M. Lehn, *Chem. Commun.* **1989**, 1016; c) A. Elabed, P. Muller, P. Peretti, F. Gallet, J. Billard, *J. de Physique II* **1993**, *3*, 851; d) M. A. Kalinina, V. V. Arslanov, S. Z. Vatsadze, *Colloid J.* **2003**, *65*, 177; e) V. Kalsani, H. Ammon, F. Jackel, J. P. Rabe, M. Schmittel, *Chem. Eur. J.* **2004**, *10*, 5481.

[19] D. G. Kurth, P. Lehmann, D. Volkmer, H. Cölfen, M. J. Koop, A. Müller, A. Du. Chesne, *Chem. Eur. J.* **2000**, *6*, 385.

[20] a) S. Liu, D. G. Kurth, D. Volkmer, *Chem. Commun.* **2002**, 976; b) S. Liu, D. G. Kurth, H. Möhwald, D. Volkmer, *Adv. Mater.* **2002**, *14*, 225.

[21] D. A. McMorran, P. J. Steel, *Tetrahedron* **2003**, *59*, 3701.

[22] P. Kele, J. Orbulescu, S. V. Mello, M. Mabrouki, R. M. Leblanc, *Langmuir* **2001**, *17*, 7286.

[23] Y. S. Kang, D. K. Lee, C. S. Lee, *J. Phys. Chem. B.* **1999**, *103*, 2035.

[24] G. L. Gaines in *Insoluble Monolayers at Liquid–Gas Interface*, P73, Interscience, New York, **1966**.

[25] X. Chen, S. Wiehle, M. Weygand, G. Brezesinski, U. Klenz, H.-J. Galla, H. Fuchs, G. Haufe, L. Chi, *J. Phys. Chem. B.* **2002**, *106*, 9341.

[26] a) S.-G. Youm, K. Paeng, Y.-W. Choi, S. Park, D. Sohn, Y.-S. Seo, S. K. Satija, B. G. Kim, S. Kim, S. Y. Park, *Langmuir* **2005**, 21, 5647; b) D. Gidalevitz, O. Y. Mindyuk, M. R. Stetzer, P. A. Heiney, M. L. Kurnaz, D. K. Schwartz, B. M. Ocko, J. P. McCauley, Jr., A. B. III Smith, *J. Phys. Chem. B.* **1998**, *102*, 6688.

[27] C. L. Claypool, F. Faglioni, W. A. Goddard III, H. B. Gray, N. S. Lewis, R. A. Marcus, *J. Phys. Chem. B* **1997**, *101*, 5978.

[28] C. Thalacker, A. Miura, S. D. Feyter, F. C. De Schryver, F. Würthner, *Org. Biol. Chem.* **2005**, *3*, 414.

[29] A. Mourran, U. Ziener, M. Möller, M. Suarez, J. M. Lehn, *Langmuir* **2006**, *22*, 7579.

[30] A. Mourran, U. Beginn, G. Zipp, M. Möller, *Langmuir* **2004**, *20*, 673.

[31] a) P. Zell, F. Mögele, U. Ziener, B. Rieger, *Chem. Commun.* **2005**, 1294; b) P. Zell, F. Mögele, U. Ziener, B. Rieger, *Chem. Eur. J.* **2006**, *12*, 3847–3857.

[32] S. De Feyter, M. M. S. Abdel-Mottaleb, N. Schuurmans, B. J. V. Verkuijl, J. H. van Esch, B. L. Feringa, F. C. De Schryver, *Chem. Eur. J.* **2004**, *10*, 1124.

[33] D. M. Cyr, B. Venkataraman, G. W. Flynn, A. Black, G. M. Whitesides, *J. Phys. Chem.* **1996**, *100*, 13747.

[34] P. Quagliotto, G. Viscardi, C. Barolo, E. Barni, S. Bellinvia, E. Fisicaro, C. Compari, *J. Org. Chem.* **2003**, *68*, 7651.

[35] G. M. Sheldrick, *SHELXL-97: Program for Crystal Structure Determination*, Universität Göttingen, Germany, **1997**.